Characterization and performance within the WGS reaction of Cu catalysts obtained from hydrotalcites

Edgardo Meza Fuentes, Johana Rodríguez-Ruiz, L. Massin, Francisco Jose Cadete Santos Aires, Arnaldo da Costa Faro, José Mansu Assaf, María Do Carmo Rangel

Characterization and performance within the WGS reaction of Cu catalysts obtained from hydrotalcites

Edgardo Meza Fuentes[1*], Johana Rodriguez Ruiz[2], Laurence Massin[3], Francisco J. Cadete Santos Aires[3,4], Arnaldo da Costa Faro Jr[5], José Mansur Assaf[6], Maria do Carmo Rangel[7]

[1]*Grupo de Estudios en Materiales y Combustibles, Campus San Pablo, Universidad de Cartagena, Cartagena, Colombia.*emezaf@unicartagena.edu.co*

[2]*Grupo de Investigación en Procesos de la Industria Petroquímica, SENA-Centro para la Industria Petroquímica, Cartagena, Colombia.*

[3]*Université de Lyon, Université Claude Bernard Lyon 1, CNRS - UMR 5256, IRCELYON 2, Avenue Albert Einstein, 69626 Villeurbanne Cedex, France.*

[4]*Laboratory for Catalytic Research, National Research Tomsk State University, 36 Lenin Avenue, Tomsk 634050, Russian Federation.*

[5]*Universidade Federal do Rio de Janeiro, Ilha do Fundão, 21941-909, Rio de Janeiro, Rio de Janeiro, Brazil*

[6]*Universidade Federal de São Carlos, Rod. Washington Luiz, Km 235, 13565-905 São Carlos, São Paulo, Brazil.*

[7]*Instituto de Química, Universidade Federal do Rio Grande do Sul. Av. Bento Gonçalves, 9500, Agronomia, 90650-001 Porto Alegre, RS, Brazil.*

Abstract

In large-scale industry, the WGS reaction is the most widely used method for the purification of hydrogen obtained from natural gas. This is a process that hinges on factors such as temperature, pressure, type of catalyst, etc. Experimentation with copper-based catalysts synthesized from HTLc-type solids can lead to enhancements in the hydrogen production processes, due to the thermal and mechanical properties of the solids that can be obtained by the calcination of such materials. In this work, copper-based solids were obtained from hydrotalcites, which were characterized through various techniques and evaluated within the WGS reaction at different temperatures. Hydrotalcite-type precursors displayed thermal behaviors that depend on their composition, whereby higher temperatures become necessary for the collapse of the HTLc structure in the solids with higher zinc and aluminum content. The catalysts were active in the reaction under study with $C_{0.50}Z_{0.25}A_{0.25}$ being the most active material due to the higher content of metallic copper on the surface. The most effective material in terms of metallic copper content present on the surface was $C_{0.33}Z_{0.33}A_{0.33}$, in which the occurrence of CuO was not evinced after its use, in addition to displaying the smallest particle size of Cu^0 as well as, possibly, the existence of Cu-Zn interactions on the surface.

Introduction

Catalytic reactions for hydrogen production are of great importance for the industrial synthesis of ammonia, hydrogenation of vegetable oils, and petrochemical processes as well as in the production of methanol, among others [1,2]. Currently, hydrogen offers a high potential for the generation of energy in fuel cells, mainly used in the transport sector [3-9]. Most of the industrial hydrogen is obtained from methane reform, and, to a lesser extent, in alternative or complementary processes such as partial oxidation, dry and autothermal methane reforms, methanol reform and biomass reform [10-17]. During the generation of hydrogen at an industrial level, a gaseous mixture is produced, which contains, among other compounds, carbon monoxide that can act as a poison for catalysts used in subsequent reactions [2]. Given this circumstance, it became necessary that the water gas shift (WGS) reaction be used as part of the hydrogen generation process from methane, which, in addition to eliminating carbon monoxide, increases hydrogen production. Before the use of reform and WGS reactions, hydrogen was produced through the addition of strong acids to metals or by means of water electrolysis [15,18]; however, these methods were difficult to control and failed to meet the growing demand for hydrogen. This need led to the development of research aimed at obtaining hydrogen through heterogeneous catalysis processes, which led to the use of nickel-based catalysts for the methane reform, and of iron-chromium for the WGS reaction. [2].

Presently, the WGS reaction is carried out in two stages: high temperature shift (HTS) and low temperature shift (LTS) in temperatures ranging between 350-450 °C and 150-250 °C, respectively [2,19-22]. The catalysts used in HTS are made from Fe_2O_4, which contains, in a lower proportion, Cr_2O_3 that acts as a textural promoter increasing both mechanical and thermal resistance, besides avoiding the sintering of the catalyst [20,23,24]. The LTS process is necessary to obtain a gaseous mixture in which the remaining carbon monoxide concentration is negligible [2,24]. In this stage, copper-based catalysts supported on Al_2O_3 are utilized to improve physical properties and to increase the dispersion of copper on the surface of the material. In addition to these catalysts, ZnO is incorporated, which acts as a structural promoter leading to increased activity and selectivity of the catalyst and performing additionally as an inhibitor of poisoning processes. [24-26].

The WGS reaction shows thermodynamic and kinetic limitations that must be considered to ensure high conversions and selectivity; therefore, the use of sintering-resistant active solids is required. This has led to the study of new materials based on gold [3,26], cerium [24,26], manganese [27], iron [28-31], nickel [32], as well as the evaluation of catalysts containing molybdenum or yttrium as dopants [33, 34], among others. By the same token, catalysts that show activity at intermediate temperatures (MTS) have been studied [35-41]. Among the materials most studied in recent years in heterogeneous

catalysis are the precursors of the hydrotalcite (HTLc) or layered double hydroxides (LDH) type, which can be made up of various metal cations and anions that confer different properties. HTLc by calcination processes can generate a wide variety of solids whose characteristics depending on their composition, presenting properties such as homogeneous particle distribution, as well as thermal and mechanical stability of solids [42,43].

In this work, catalysts of the $Cu/ZnO/Al_2O_3$ type prepared from hydrotalcites were studied. The materials obtained were characterized by using different instrumental techniques and evaluated in the WGS reaction at temperatures between 150 and 350 °C.

Experimental

The catalysts were obtained from the calcination of hydrotalcites prepared by the low saturation method at a constant pH. For the synthesis of hydrotalcites, saline solutions based on copper nitrate were used. [$Cu(NO_3)_2 \cdot 6H_2O$], zinc nitrate [$Zn(NO_3)_2 \cdot 6H_2O$] and aluminum [$Al(NO_3)_3 \cdot 9H_2O$], as well as alkaline solutions containing potassium hydroxide (KOH) and potassium carbonate (K_2CO_3) [28,30]. The molar ratios of the Cu^{2+} and Zn^{2+} cations, as well as $(CO_3)^{2-}$ and OH^- anions were adjusted based on the fixed use of 0.05 moles of the Al^{3+} cation in order to synthesize the $Cu_{0.50}Zn_{0.25}Al_{0.25}(OH)_2(CO_3)_{0.125}$, $Cu_{0.37}Zn_{0.37}Al_{0.25}(OH)_2(CO_3)_{0.125}$, $Cu_{0.44}Zn_{0.22}Al_{0.33}(OH)_2(CO_3)_{0.125}$ and $Cu_{0.33}Zn_{0.33}Al_{0.33}(OH)_2(CO_3)_{0.125}$ materials, in which the subscripts indicate the molar ratios of the species present in each material. During the synthesis, the saline and alkaline solutions were mixed in a controlled manner by maintaining the pH at 8.3-8.4 throughout the process. The solids formed were filtered, washed with deionized water, and dried at 60 °C for 24 h. Subsequently, the materials were calcined at 500 °C under an air flow of 100 ml / min for 4 hours. The solids obtained were characterized by thermogravimetric analysis (TGA-DTA), X-ray diffraction (XRD), Fourier transform infrared spectroscopy (FTIR), specific surface area measurement by the BET method as well as porosity by the BJH method, reduction at a set temperature (RST), copper dispersion measurements and X-ray photoelectron spectroscopy (XPS).

The TGA and DTA analyzes were performed on the precursors of the hydrotalcite type, using a TA Instruments SDT 2670. In these experiments 15 mg of samples were used, which were heated at a rate of 10 °C·min^{-1} from 30 to 800 °C, under air flow of 50 mL·min^{-1}.

The X-ray diffraction (XRD) patterns of hydrotalcites were recorded in a Bruker D8 Advance with CuKα radiation (λ= 1.54059 Å) generated at 40 kV and 40 mA in the 5-80° (2θ) range. The X-ray

diffraction patterns of the calcined (10-80°, 2θ range) and spent catalysts (20-80°, 2θ range) were recorded in Rigaku Multiflex, with CuKα radiation (λ= 1.54059 Å), generated at 40 kV and 40 mA. The specific surface area and porosity of calcined solids were determined by BET (Brunauer-Emmett-Teller) and BJH (Barrett-Joyner-Halenda) methods respectively. These parameters were measured through adsorption/desorption of nitrogen at 196.15 °C, using a Micromeritics ASAP 2010 instrument. Prior to analysis, 0.2 g of samples were heated up to 200 °C under vacuum (2 mm Hg) to remove water and volatile matter.

The temperature-programmed reduction experiments were performed in a Zeton Altamira AMI 90 instrument, equipped with TCD detector. In this analysis, 0.05 g of samples were heated up to 300 °C to remove water and impurities and subsequently cooled down to 25 °C. During analysis, the samples were heated from 25 to 500 °C under 5% H_2/Ar flow of 50 mL·min^{-1}.

X-ray photoelectron spectroscopy (XPS) analyses were performed on samples $C_{0,44}Z_{0,22}A_{0,33}$ and $C_{0,33}Z_{0,33}A_{0,33}$, in a Kratos Axis Ultra DLD spectrometer, using monochromated AlKα rays as the excitation source. Survey scans were performed using a pass energy of 160 e, and the specific regions (O1s, C1s, Cu2p, Zn2p, Al2p) were recorded at a pass energy of 20 eV to obtain a better peak resolution. In XPS calibration of the energies requires information on the origin of the energy scale (0 eV) that is provided (on conducting materials) by recording the valence band and measuring the Fermi level of the analyzer [44,45]. As it is unreliable to try to measure the Fermi energy level of the analyzer with poorly conducting materials such as ours we can minimize measurement inaccuracies of the binding energies (BEs) by calibrating all peaks with respect to an internal reference to the material. This reference can be either a building block of the material [46,47] or adventitious contamination carbon [48,49]; in our case we would ideally consider the Al2p peak but unfortunately there is a contribution of copper (Cu3p) near Al2p peak which renders the precise positioning of this peak rather hazardous. We have thus chosen the second solution and referenced the BEs to the principal component of the peak-fitted C1s envelope, arbitrarily assigned the often used [50,51] and consistently independently measured with our spectrometer [49] value of 284.6 eV, characteristic of C-(C,H) bonds. Shirley background subtraction and peak fitting to relevant Gaussian-Lorentzian functions were realized on each acquired spectrum prior to any measurements.

For dispersion and metallic area of cooper measurements, the solids were previously reduced using a 5% H_2/N_2 flow, from 25 to 350 °C and heating rate of 10 C min^{-1}. Once this step was done, the samples were maintained for 1 h at 350 °C, registering the hydrogen consumption. These conditions were used to simulate those used during the copper catalysts reduction prior to the catalytic evaluation. Subsequently the solids were then cooled to 90 °C and oxidized with nitrous oxide in a

flow of 30 $mL \cdot min^{-1}$, for 80 min. The ratio of hydrogen consumption before and after oxidation nitrous oxide was used to calculate the copper dispersion. The metallic area of copper of the solids was determined by the number of copper atoms per unit surface area (1.47×10^{19} atom Cu/m^2).
The turnover frequency (TOF) was calculated using the number of moles of carbon monoxide converted as a function of the number of moles of Cu° obtained from the metallic area by the time unit.

For the activation of the copper catalysts, 100 mg of the solids were reduced using a 100 $mL \cdot min^{-1}$ flow of 10 % H_2/N_2 mixture at 350 ° C for 1 hr. After this step, the solids were evaluated in the WGS reaction of 150 to 350 °C range and 1 atm of pressure. In catalytic evaluation, a flow of water vapor/CO=10 molar ratio was used. This mixture was obtained by passing a 10 % CO/N_2 flow of 60 $mL \cdot min^{-1}$ for water vapor generated through of the dosage of water liquid using a pump in a vaporizer at 303 °C. The quantification of gases used and generated during the reaction, was performed using a gas chromatograph Varian Model 3800, equipped with a Porapak column and molecular sieve and two TCD detectors.

Results and Discussion

The hydrotalcite type structure (JCPDS card 89-0460) was confirmed in all solids through the peaks recorded in the X-ray diffraction patterns shown in Figure 1. The solids with the Cu / Zn = 1 molar ratio presented more defined peaks than those present in materials with higher copper content, where the peak corresponding to the crystallographic plane was observed in the ($Cu_{0.37}Zn_{0.37}Al_{0.25}$ and $Cu_{0.33}Zn_{0.33}Al_{0.33}$) solids (110). In the $Cu_{0.50}Zn_{0.25}Al_{0.25}$ material, a peak attributable to the $Cu(OH)_2$ phase was recorded, which is probably due to the Jahn-Teller effect seen in high copper hydrotalcites [52,53].

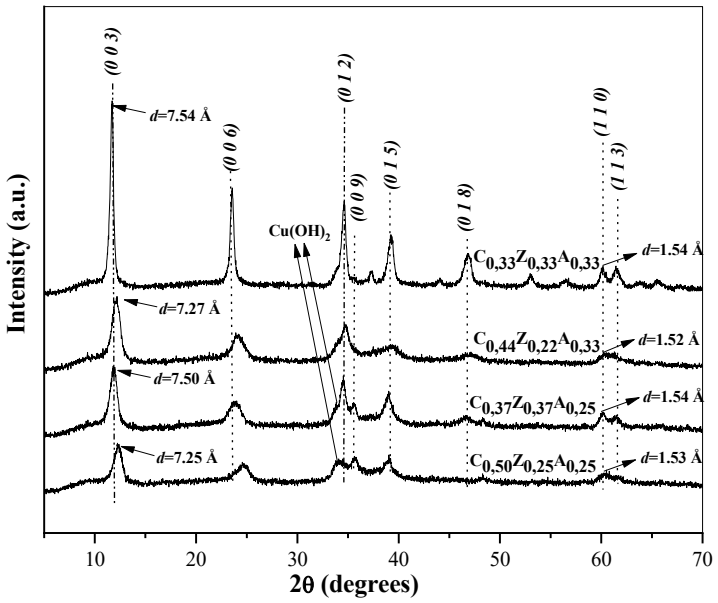

Figure 1. X-ray diffractograms of solids before calcination process.

In the mass loss curves of the hydrotalcite type precursors, shown in Figure 2, four mass loss zones can be observed, which are associated with; (I) the exit of water molecules located on the surface of the materials and in the interlaminar regions, (II) the beginning of the decomposition of interlaminar anions and with the collapse of the hydrotalcite type structure, (II) the decomposition of hydroxide groups and formation of divalent metal oxides (CuO, ZnO) at low temperature and trivalent ones at higher temperature (Al_2O_3, ≥ 450°C), and (IV) the continuation of aluminum oxide formation and the exit of water and carbon dioxide that were trapped in the pores due to the simultaneous processes of collapse of the HTLc-type structure and the decomposition of the OH and CO_3^{2-} anions by effect of temperature.

It was observed that materials with higher copper content collapse at lower temperatures (142 °C for $C_{0.50}Z_{0.25}A_{0.25}$ and 157 °C for $C_{0.44}Z_{0.22}A_{0.33}$). This may be due to the presence of $Cu(OH)_2$ in these materials or to the lower interplanar distance reached by these materials through the values of the *c* parameter (Table 1). For materials with lower copper content ($C_{0.37}Z_{0.37}A_{0.25}$ and $C_{0.33}Z_{0.33}A_{0.33}$), there is wider separation between units of the Cu^{2+} type within the hydrotalcite structure, thus decreasing the Jahn-Teller effect and increasing the thermal stability of these materials. The solids with the highest aluminum content achieved the greatest mass loss in zones I, II and IV, a fact that may be related to the high-water adsorption capacity of aluminum oxyhydroxides. All the materials reached an abrupt loss of mass at temperatures above 570 °C, probably due to the exit of carbon dioxide and water molecules that were trapped in closed spaces within the solids due to the collapse of the

structure at low temperatures as well as through the formation of metal oxides from the decomposition of the hydroxide groups present in the initial structure [54].

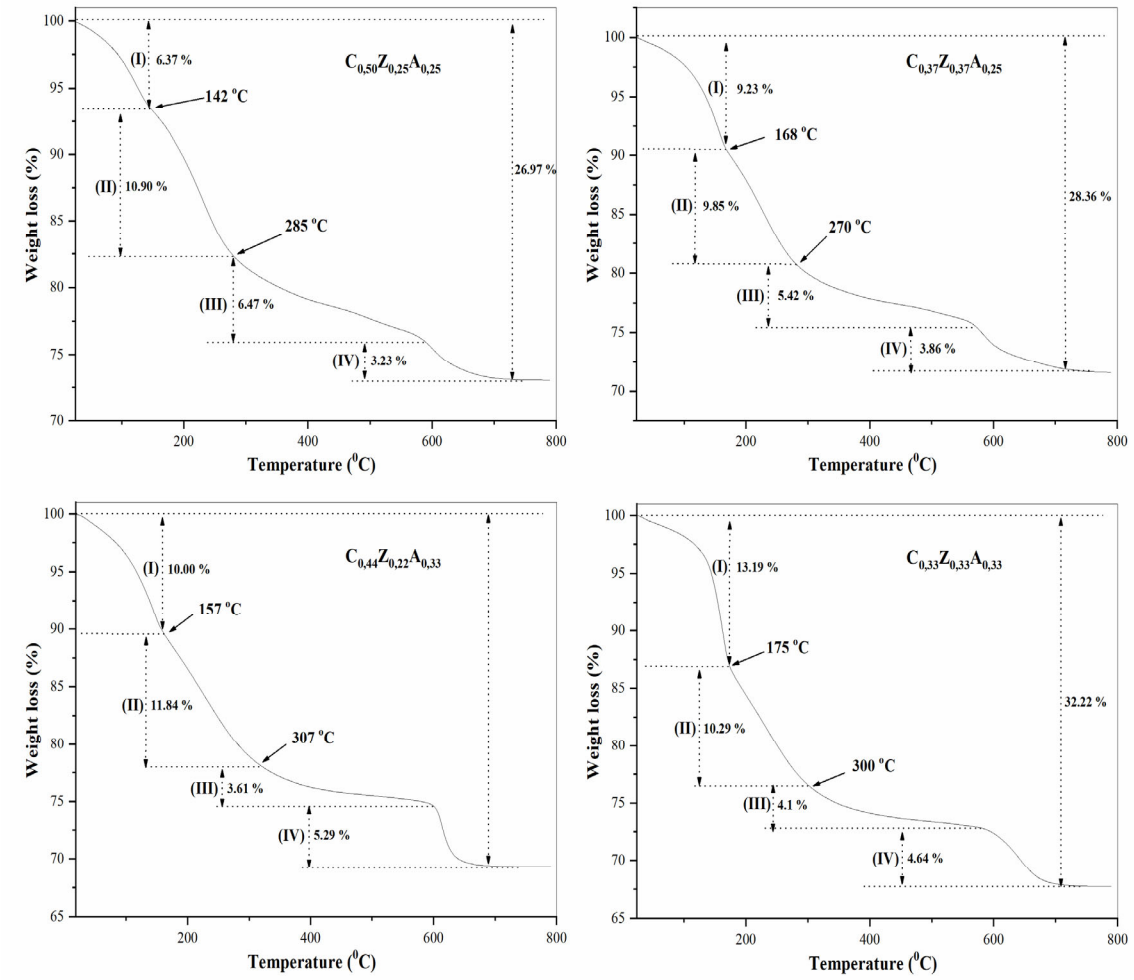

Figure 2. Thermogravimetry curves of hydrotalcite-type precursors.

Table 1. Values of interplanar distance (ID), collapse temperature (CT), and mass loss (ML) associated with events recorded in the TGA curve of hydrotalcite-type precursors.

Sample	ID (Å)*	CT (ºC)	ML Step I	ML Step II	ML Step III	ML Step IV
$C_{0.50}Z_{0.25}A_{0.25}$	21.76	142.0	6.37 %	17.27 %	23.74 %	26.97 %
$C_{0.37}Z_{0.37}A_{0.25}$	22.48	168.0	9.23 %	19.08 %	24.50 %	28.36 %
$C_{0.44}Z_{0.22}A_{0.33}$	21.81	155.9	10.01 %	21.84 %	25.45 %	30.74 %
$C_{0.33}Z_{0.33}A_{0.33}$	22.63	175.0	13.19 %	23.48 %	27.58 %	32.22 %

* The values of the interplanar distance (ID) were calculated through the peak attributed to the plane (0 0 3) in the X-ray diffractograms of the precursors with hydrotalcite type structure.

Figure 3 contains the X-ray diffractograms of the solids calcined at 500 °C. The presence of the CuO and ZnO phases, resulting from the decomposition of hydrotalcites, was mainly perceived in materials with lower aluminum content. In materials in which the aluminum content is higher, diffraction patterns shown broad and poorly defined peaks, which may be produced by the increase in the amorphous character of the solids due to the presence of transitional alumina.

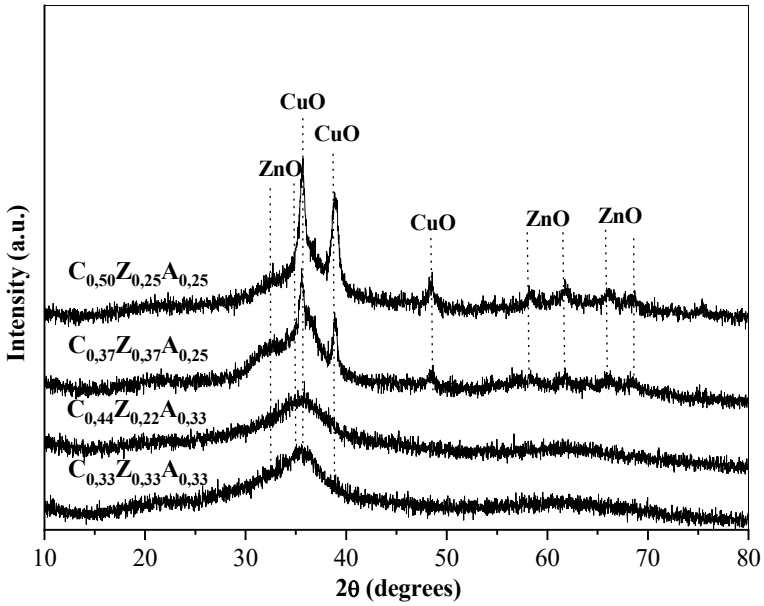

Figure 3. X-ray diffractograms of solids obtained from calcination at 500 °C of the hydrotalcites.

The adsorption-desorption isotherms of the materials displayed similar profiles, which reflect the presence of lumped particles in the form of sheets that originate pores in the form of notches, which conform to the type II isotherms as per the IUPAC classification (Figure 4a) [55].

The narrow hysteresis loops that were registered by the adsorption-desorption graphs point out to the presence of mesopores, which is confirmed by the pore distribution shown in Figure 4b. All materials contain pores between 2 and 75 nm, and a mean radius that slightly decreases in samples with higher aluminum content. The values in Table 2 indicate that the $C_{0.50}Z_{0.25}A_{0.25}$ material has the largest pore diameter and volume, as well as the highest specific surface area (69 m^2/g); this is probably due to the fact that, in this solid, the number or length of the pores is greater than that accomplished by the other samples, which leads to an increase in the surface area.

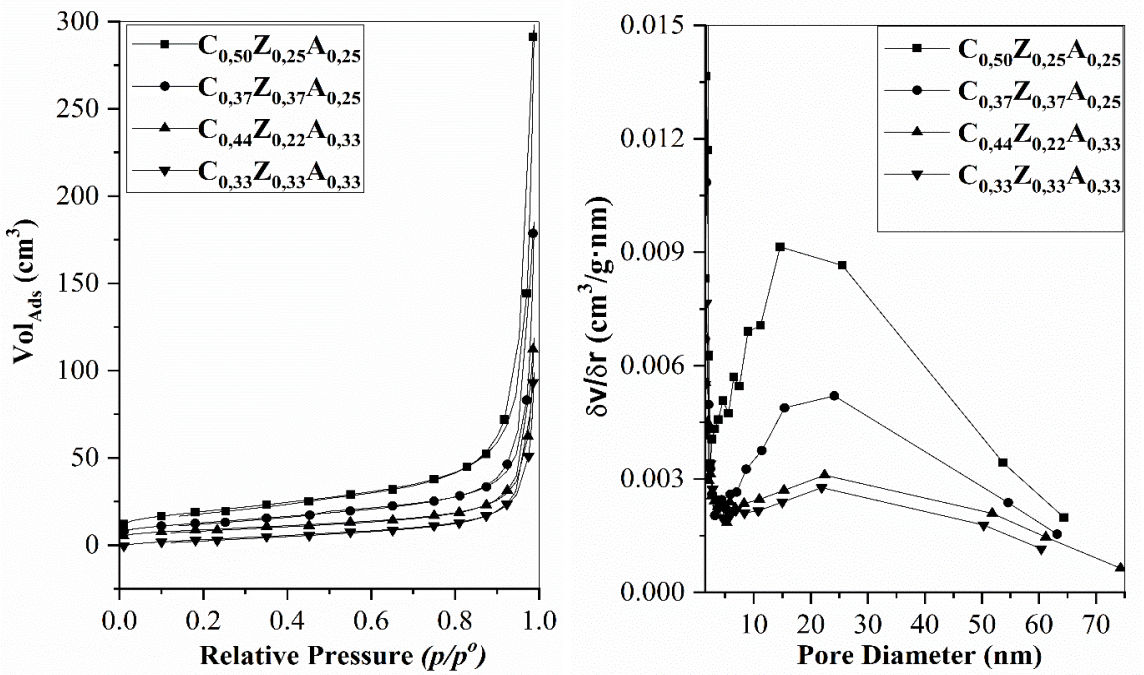

Figure 4. Isotherms of adsorption-desorption of nitrogen at 77 K and pore distribution of the calcined solids.

The TPR graphs, shown in Figure 5, display a single reduction peak, which is attributable to the CuO present in all the calcined solids [56,57]. It was observed that the material with the highest copper content ($C_{0.50}Z_{0.25}A_{0.25}$) achieved the lowest reduction temperature, with a peak centered at 225 °C and extending to 270 °C. In the case of the other materials, the temperature required to reduce CuO to Cu^0 was higher, which indicates that the hike in aluminum content makes the copper reduction process difficult, in a way similar to that observed in the case of other metal cations [57,58]. Such results suggest that the $C_{0.50}Z_{0.25}A_{0.25}$ material contains the highest content of CuO on the external surface, which facilitates its reduction at low temperatures, whereas, in solids with higher aluminum content, CuO is located mainly in the internal volume of the materials, which makes the prior diffusion of the hydrogen necessary to react with CuO. This fact is confirmed by the metallic dispersion values shown in Table 2, in which it can be seen that the solids with the lowest aluminum proportion have the highest copper dispersion on the surface, which favors the reduction reaction at low temperatures. The $C_{0.50}Z_{0.25}A_{0.25}$ material showed the highest metallic copper area, with a value close to the specific surface area reached by this material, which confirms a higher proportion of CuO on the surface for this material, when compared to the other solids studied.

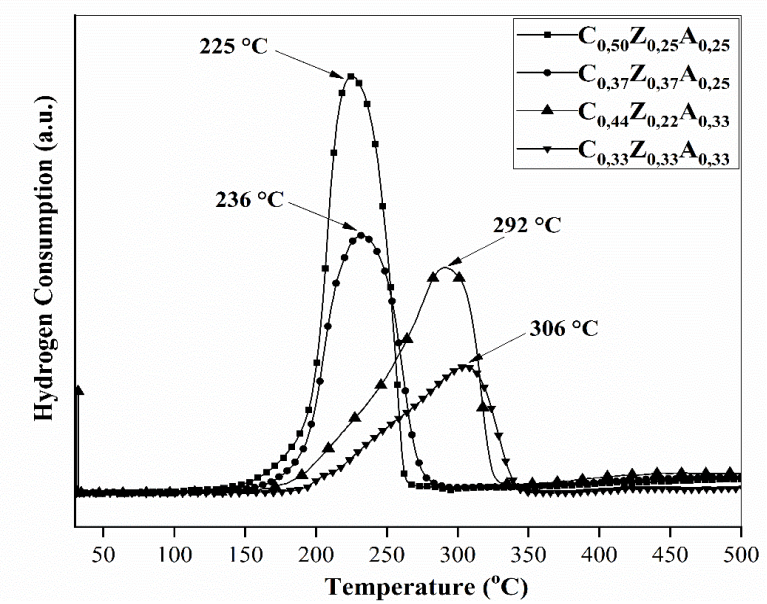

Figure 5. Curves of temperature programmed reduction of solids after calcination.

Table 2. Values of the specific surface area (Sg), average pore radius and pore volume of calcined solid; dispersion and metallic area of copper reduced using conditions similar to those used before the catalytic evaluation.

Sample	Sg (m^2/g)	Pore diameter (nm)	Pore volume (cm^3/g)	Metallic area (m^2/g)	Particle size (nm)	Dispersion (%)
$C_{0.50}Z_{0.25}A_{0.25}$	69	13.35	0.46	60.7	12.9	39.2
$C_{0.37}Z_{0.37}A_{0.25}$	46	11.84	0.29	36.6	13.4	40.0
$C_{0.44}Z_{0.22}A_{0.33}$	36	10.48	0.18	25.2	4.6	25.0
$C_{0.33}Z_{0.33}A_{0.33}$	33	10.36	0.16	14.9	4.4	22.4

* Specific surface area (Sg), average pore radius and pore volume were obtained by adsorption-desorption of nitrogen at 77 K; dispersion and metallic area of copper were obtained by reduction with hydrogen, previous surface oxidation with nitrous oxide of CuO present in the calcined solids; particle size of the metallic copper were calculated using the Scherrer equation and the plane (*1 1 1*) of the Cu^0 crystal lattice obtained from the XRDs of the catalysts used.

All the catalysts were active for the WGS reaction, though the formation of species other than hydrogen and carbon dioxide was not observed. Figure 6a comes to show that the conversion percentage increases with temperature, being $C_{0.50}Z_{0.25}A_{0.25}$ the most active solid up to 250 ° C, while, at higher temperatures, the $C_{0.37}Z_{0.37}A_{0.25}$ solid led to higher percentages of monoxide to carbon dioxide conversion through the WGS reaction, reaching values close to 90% conversion. In the case of catalysts with higher aluminum content, the conversion was lower, which may be due to the lower specific surface of such materials. It was observed that, in materials with the same aluminum content, catalysts with a Cu/Zn molar ratio equal to 1 are more active, which can be attributed to the fact that zinc also contributes to the WGS reaction [59]. This effect is more evident in the turnover frequency

curves (TOF, Figure 6b), in which it is verified that the catalysts with this Cu / Zn molar ratio are more efficient, even when the metallic area for such solids is less than that shown for the $C_{0,50}Z_{0,25}A_{0,25}$ catalyst.

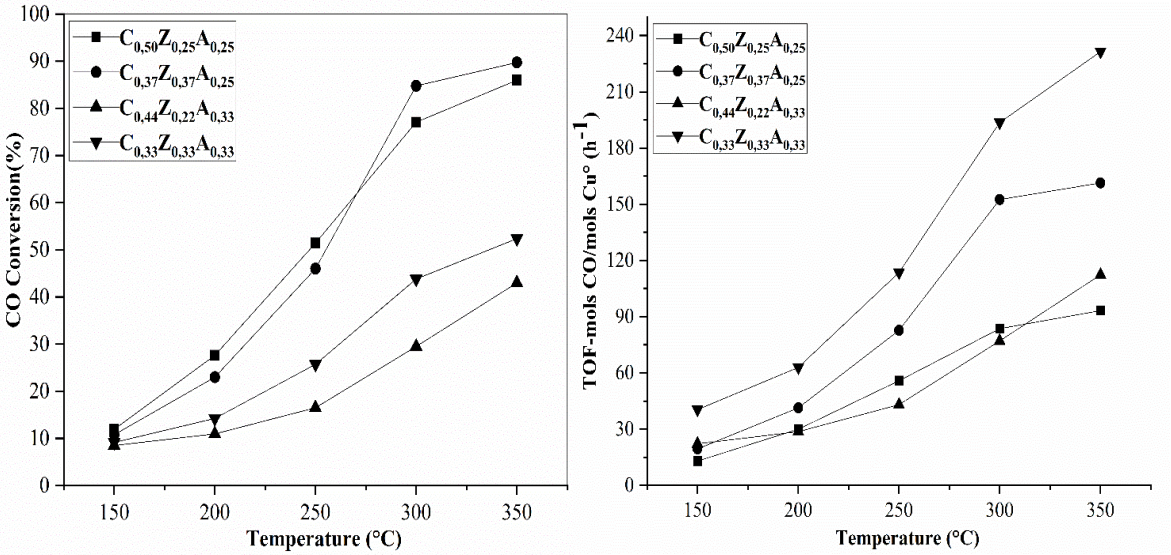

Figure 6. Conversion and turnover frequency (TOF) of monoxide to carbon dioxide through the WGS reaction using calcined catalysts, after reduction with hydrogen at 350 °C.

XPS was performed $C_{0.44}Z_{0.22}A_{0.33}$ and $C_{0.33}Z_{0.33}A_{0.33}$ materials after the process of reduction with hydrogen. In the literature, XPS studies on (Cu,Zn,Al) hydrotalcite [50], on mixed Cu-Zn-Al mixed oxides [60-63] or even on copper aluminates [51,64-66] generally concentrate the information given on Cu and Zn (often the Cu2p and Zn2p BE regions) and only seldom give information on Al (Al2p BE region); indeed only a few measurements of the Al2p BE are given in the case of copper aluminates [51,66]. In the case of copper aluminates, either [64] or [66] are often referred to as references for data on $CuAl_2O_4$. Occasionally Al2p BE is rather used as energy reference instead of the BE of C-(C,H) bonds in adventitious carbon; the assigned value can vary from 74,0 eV [64] to 74.5 eV [60]. Actually the latter value is also derived from data on $CuAl_2O_4$ where the reference energy corresponding to BE of C-(C,H) bonds in adventitious carbon was taken to be 285.1 eV [66] instead of the more often used 284.6 eV [49-51]. This is important when comparing data on the BE measured for the different components of the material since it introduces a 0.5 eV shift in this data. In the following we will take this into account and will explicitly inform when the data was corrected for this shift.

The spectra obtained for both samples for aluminum (Al2p), copper (Cu2p) and zinc (Zn2p) are shown in Figure 6. Data extracted from these spectra is available in Tables 3 (BEs), 4 (surface

composition) and 5 (relative content of the components used for fitting the experimental peaks). We can notice that in binding energy (BE) region of the Al 2p peak (Figure 6a) there is a high BE contribution arising from the presence of the Cu3p peak within the same BE region. Although this may be hazardous if one wants to use the BE of Al2p as the reference energy, it does not (strongly) affect the determination of the BE of Al2p which was measured to be 73.8 eV for both samples. This is in good agreement with Al2p BE found either in copper aluminates or CuAlZn hydrotalcites. As mentioned above, only a few measurements of the Al2p BE are given in the case of copper aluminates: for $CuAlO_2$ the value given is 74±0.5 eV [51] (in this reference, variation in BE is due to Eu cation doping) and for $CuAl_2O_4$ the value given is 74.5 eV [66]; the latter value corrected for the shift in the reference energy mentioned above (-0.5 eV) is thus also around 74 eV.

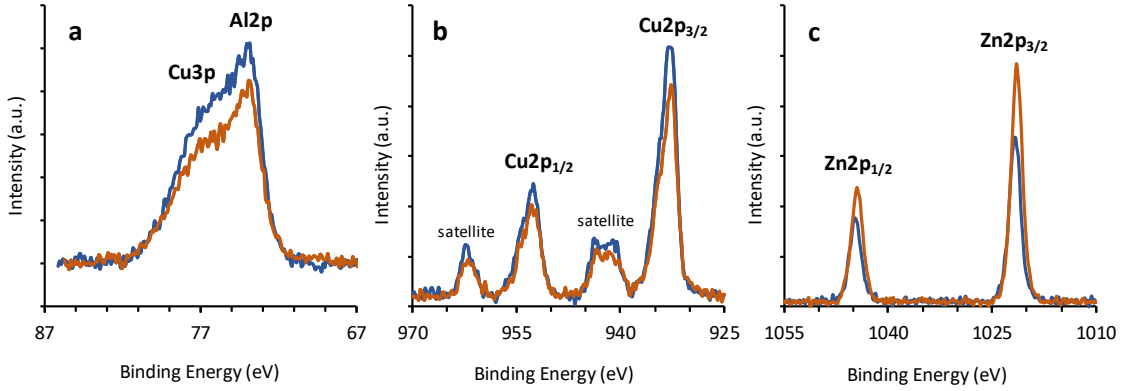

Figure 6. XPS of the reduced $C_{0.44}Z_{0.22}A_{0.33}$ (orange spectra) and $C_{0.33}Z_{0.33}A_{0.33}$ (blue spectra) catalysts: (a) Cu3p, Al2p BE region; (b) Cu2p BE region and (c) Zn2p BE region.

XPS spectra of the Cu2p and Zn2p BE regions are presented in Figures 6b and 6c and respectively; more detailed data for these regions are available in Figure 7 where decompositions of the $Cu2p_{3/2}$-$Cu2p_{1/2}$ (Figure 7a) and $Zn2p_{3/2}$-$Zn2p_{1/2}$ (Figure7b) are provided. The main features are similar for both samples. Spectra of Cu2p present $Cu2p_{3/2}$ and $Cu2p_{1/2}$ peaks with a main component and one or two high BE energy shoulders; a key feature is the presence of satellites characteristic of Cu^{2+} in CuO [67-72], $Cu(OH)_2$ [67,69-71,73], $CuAl_2O_4$ [61,65,66] and (Cu,Zn,Al)HT [50] and which is extremely faint (even non-existent) in Cu_2O [69-72,74] and Cu [69-71,75]. Thus the presence of strong satellites rules out the possibility of the presence of Cu_2O in the sample. A close view of satellite present just after the $Cu2p_{3/2}$ peak exhibit two shoulders (black and grey arrows in Figure 7a) which are characteristic of CuO [68-72] and $CuAl_2O_4$ [61,65,66]; these shoulders are absent for $Cu(OH)_2$ [69-71,73], and (Cu,Zn,Al)HT [50] for which only a broad peak exists. Also, despite the noise in the

spectra we can also advance that for $C_{0.33}Z_{0.33}A_{0.33}$ catalyst the low BE shoulder (grey arrow in Figure 7a) in this satellite is more marked than for $C_{0.44}Z_{0.22}A_{0.33}$ catalyst indicating that the ratio between $CuAl_2O_4$ and CuO is certainly lower for the latter catalyst since the prominence of this low BE shoulder in this satellite is more marked in $CuAl_2O_4$ than in CuO. This qualitative observation indicates thus the presence of CuO and $CuAl_2O_4$ in the samples with variations of the relative amounts of these two components.

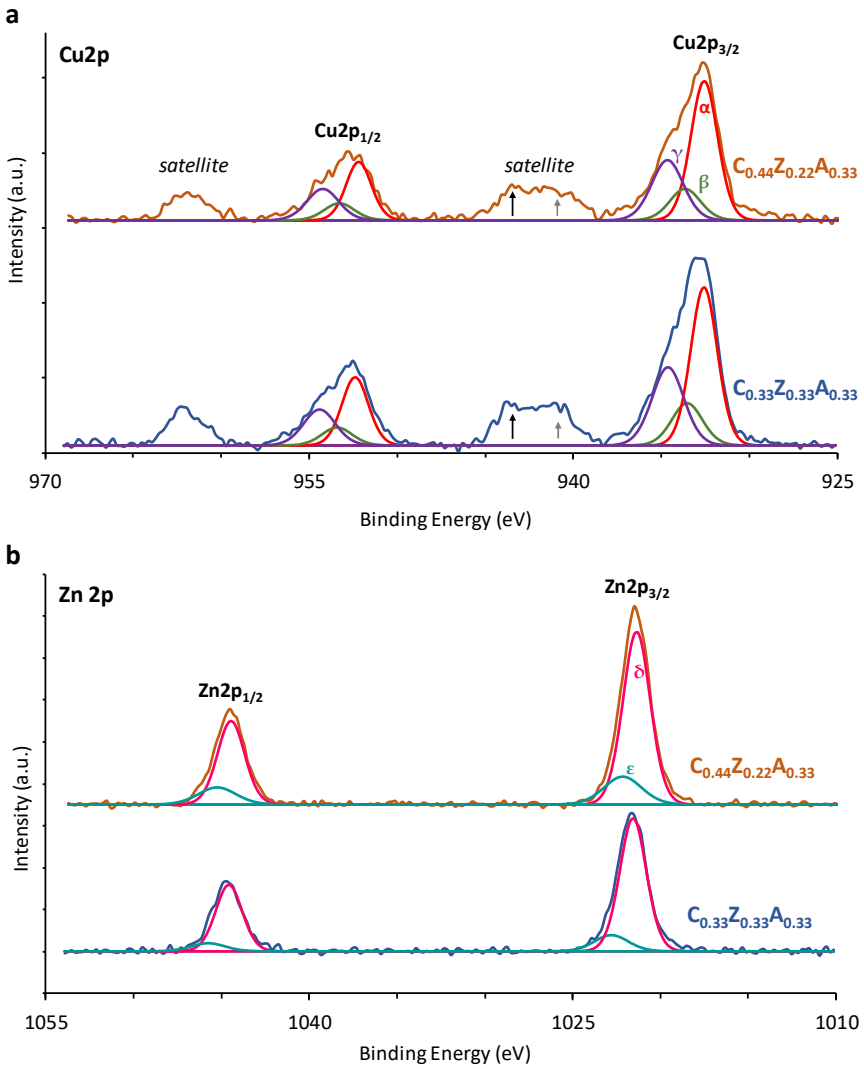

Figure 7. XPS of the reduced $C_{0.44}Z_{0.22}A_{0.33}$ (orange spectra) and $C_{0.33}Z_{0.33}A_{0.33}$ (blue spectra) catalysts: (a) $Cu2p_{3/2}$ and $Cu2p_{1/2}$ and corresponding decomposition peaks (α, β, γ – see text for details), arrows in the low BE satellite are commented in the text; (b) $Zn2p_{3/2}$ and $Zn2p_{1/2}$ and corresponding decomposition peaks (δ, ε – see text for details).

Table 3. Experimental BE of the principal peaks (P) and shoulders (high energy S_{HE}, low energy S_{LE}) and BE components used for the best fit for $Cu2p_{3/2}$, $Zn2p_{3/2}$ and O1s (see text and Figures 7 and 8 for details) of the two reduced catalysts: $C_{0.33}Z_{0.33}A_{0.33}$ and $C_{0.44}Z_{0.22}A_{0.33}$. For Al2p the experimental BE value is given in the text.

Catalyst	$Cu2p_{3/2}$ BE (eV)						$Zn2p_{3/2}$ BE (eV)			O1s BE (eV)				
	Exp			*Fit*			Exp	*Fit*		Exp		*Fit*		
	P	S_{HE-I}	S_{HE-II}	α	β	γ	P	δ	ε	P	S_{LE}	η	θ	ν
$C_{0.33}Z_{0.33}A_{0.33}$	932.8	933.7	934.7	*932.6*	*933.6*	*934.6*	1021.5	*1021.6*	*1022.8*	531.3	529.6	*529.6*	*530.5*	*531.4*
$C_{0.44}Z_{0.22}A_{0.33}$	932.7	933.8	934.8	*932.6*	*933.6*	*934.6*	1021.7	*1021.4*	*1022.1*	531.4	529.6	*529.6*	*530.5*	*531.4*

Since we have a better signal/noise ratio for the $Cu2p_{3/2}$ peak we will concentrate on this peak for the numerical data (see Tables 3, 4 and 5) extracted from the spectra and its discussion; we have verified that these measurements are consistent with the data for $Cu2p_{1/2}$. For the two samples we have similar characteristics for the $Cu2p_{3/2}$ peak: a main peak with two high BE shoulders indicating the presence of at least three components. In the experimental spectra the main peak is centred at 932.7 eV for $C_{0.33}Z_{0.33}A_{0.33}$ and at 932.8 eV for $C_{0.44}Z_{0.22}A_{0.33}$. The two high BE energy shoulders are at around 933.8 eV and 934 eV for $C_{0.33}Z_{0.33}A_{0.33}$ and at around 933.7 eV and 934.7 eV for $C_{0.44}Z_{0.22}A_{0.33}$. These values correlate well with values from literature for Cu(0) at around 932.6±0.2 eV [69,71,72], CuO at around 933.6±0.4 eV [69,71,72] and for either $CuAl_2O_4$ [61,65,66] or (Cu,Zn,Al)HT [50] at around 934.6 eV (value corrected by -0.5eV when the energy reference was 285.1eV for C1s and consequently 74.5 eV for Al2p). Since from the qualitative analysis of the satellites we determined that the most probable attribution is $CuAl_2O_4$ rather than (Cu,Zn,Al)HT we will only consider the former in the following.

Table 4. Surface composition* determined by XPS for reduced catalysts $C_{0.33}Z_{0.33}A_{0.33}$ and $C_{0.44}Z_{0.22}A_{0.33}$.

Catalyst	Cu2p (%)	Zn2p (%)	Al2p (%)
$C_{0.33}Z_{0.33}A_{0.33}$	24.2	35.6	40.1
$C_{0.44}Z_{0.22}A_{0.33}$	32.1	26.0	41.9

* In order to directly compare the surface composition (contents in Cu, Zn and Al) of the catalysts with the bulk composition (contents in Cu, Zn and Al) we have exclude O from the quantification despite it being a component of the catalyst; the value found was quite similar (50.0±0.5%) for both samples We have also excluded C from the quantification since it is due to pollution and as such it is not part of the catalyst; the value found was also quite similar (12.5±1.0%) for both samples.

Table 5. Quantification on the different components of $Cu2p_{3/2}$, $Zn2p_{1/2}$ and O1s for the two reduced catalysts $C_{0.33}Z_{0.33}A_{0.33}$ and $C_{0.44}Z_{0.22}A_{0.33}$.

Catalyst	$Cu2p_{3/2}$ α (%)	$Cu2p_{3/2}$ β (%)	$Cu2p_{3/2}$ γ (%)	$Zn2p_{3/2}$ δ (%)	$Zn2p_{3/2}$ ε (%)	O1s η (%)	O1s θ (%)	O1s ν (%)
$C_{0.33}Z_{0.33}A_{0.33}$	52.6	16.1	31.3	86.2	13.8	18.7	2.2	79.1
$C_{0.44}Z_{0.22}A_{0.33}$	56.4	14.6	29.0	81.8	18.2	8.8	2.4	88.8

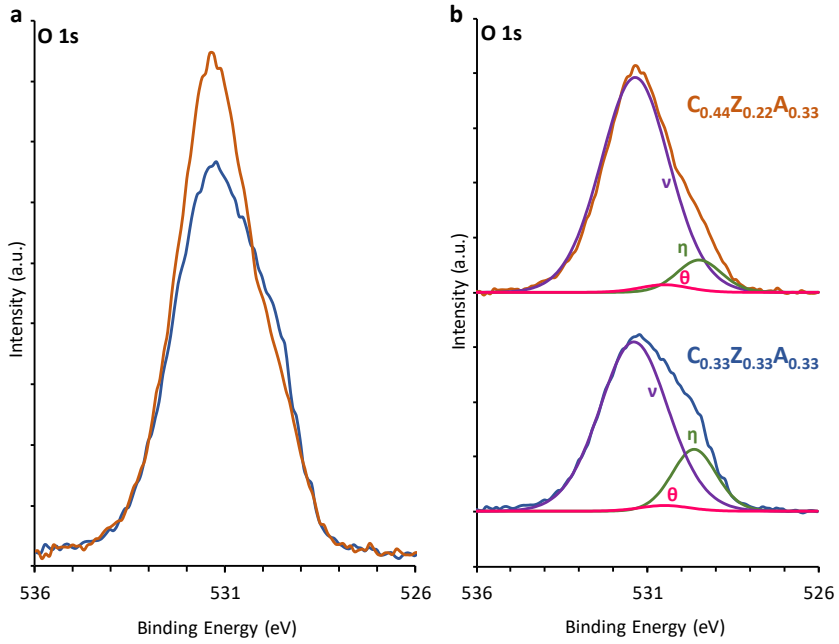

Figure 8. XPS of the reduced $C_{0.44}Z_{0.22}A_{0.33}$ (orange spectra) and $C_{0.33}Z_{0.33}A_{0.33}$ (blue spectra) catalysts: (a) O1s BE region; (b) O1s and corresponding decomposition peaks (η, θ, ν – see text for details).

We have thus used these literature values to determine the BE of the three components (α, β, γ) and realize a consistent fit of peaks $Cu2p_{3/2}$ and $Cu2p_{1/2}$ (we did not fit the satellites, for which we made a qualitative comment above, since there was no quantitative data to be extracted and to simplify Figure 7). Since we have used fixed BEs for the three components (α, β, γ) for both catalysts, we can see that the experimental BE (P, S_{HE-I}, S_{HE-II}) are slightly higher (see Table 3), although within the expected variations from literature. This very small shift, as expected from metal-metal interaction, may alos hint at Zn-Cu interaction within the three different components. This is particularly the case for the α component attributed to Cu(0) which is also detected by XRD. After reduction, we have thus the presence of metallic Cu in both catalysts with a slightly higher relative content for the catalysts richer in Cu (Table 5); this Cu domains might be slightly modified by the presence of Zn leading to the formation of intermetallics or at least C-Zn bonds. The β component, which is the minor contribution for both catalysts, was attributed to Cu(II) in CuO and the γ component to Cu(II) in $CuAl_2O_4$. Crystalline CuO was detected for $C_{0.44}Z_{0.22}A_{0.33}$ but not for $C_{0.33}Z_{0.33}A_{0.33}$ and $CuAl_2O_4$ was not detected for both by XRD. These components are either in a poorly crystalline form or are only

characteristic of the surface of the catalysts. Furthermore, we can see that the contribution from $CuAl_2O_4$ is larger than that of CuO which consistent with both the evolution of the (C,Zn,Al)HT initial material during temperature treatments and the consecutive reduction process undergone by the catalysts. We have also to consider the presence of Zn in substitution of Cu within those components leading to both mixed oxides ($Cu_{1-x}Zn_xO$) or mixed aluminates ($Cu_{1-x}Zn_xAl_2O_4$) indicating a close interaction between Cu and Zn. This seems favoured by the increasing content of Zn in the catalysts and thus more pronounced in $C_{0.33}Z_{0.33}A_{0.33}$ than in $C_{0.44}Z_{0.22}A_{0.33}$.

The analysis of the $Zn2p_{3/2}$ and $Zn2p_{1/2}$ peaks decomposition is somewhat less straightforward since the chemical shift in Zn is quite small leading to BE values very similar for Zn(0) and Zn(II) in ZnO [50,61,62,67,71,76-81] or even for Zn(II) in $ZnAl_2O_4$ [61,62,76], (Cu,Zn,Al) mixed oxides [61-63,76, 82-84] or (Cu,Zn,Al)HT [50]. Indeed, the consulted literature gives values, for $Zn2p_{3/2}$ BE, around 1021.7±0.8 eV (when necessary BE values were corrected by -0.5eV when the energy reference was 285.1eV for C1s and consequently 74.5 eV for Al2p) for all these compounds; and even contradictory chemical shifts ($BE_{ZnO} < BE_{Zn}$) were found [71]. It is thus very difficult to differentiate those compounds without information on the Auger parameter [85]; we could not calculate the latter since we could not gather reliable information on the the LMM Zn Auger lines. However for the (Cu,Zn,Al) mixed oxides a tendency was observed where the BE would increase with increasing Al content [61,62]. Considering all this we have thus decided not to fix the BE of the components used to fit the $Zn2p_{3/2}$ peak, as we did previously for $Cu2p_{3/2}$. For both samples the $Zn2p_{3/2}$ peak is constituted by a single principal peak (P) with no apparently detectable high BE shoulders (Figure 6c and Figure 7b). However, the best fit (Figure 7b) was obtained by a combining a principal component (δ) associated with a very small high BE component (ε) accounting for a slight high BE asymmetry. The component δ was found to have a similar BE for both samples (see Table 3): 1021.4 eV and 1021,6 eV for $C_{0.44}Z_{0.22}A_{0.33}$ and $C_{0.33}Z_{0.33}A_{0.33}$, respectively. Conversely, the BE of component ε has been found to be rather different (see Table 3): 1022.1 eV and 1022.8 eV for $C_{0.44}Z_{0.22}A_{0.33}$ and $C_{0.33}Z_{0.33}A_{0.33}$, respectively. The BE of the two components are both higher (slightly in the case δ of and strongly in the case of ε) for the catalysts containing the higher amount of Zn ($C_{0.33}Z_{0.33}A_{0.33}$) hinting at a stronger Cu-Zn interaction for this catalyst.

The O1s peak (Figure 8 and Table 3) is composed by a principal peak (P) with a low BE shoulder (S_{LE}). However, the best fit (Figure 8b) requires three components (η, θ, ν), the component θ being very minor (less than 3%, see Table 5); the latter corresponds to the ZnO contribution with a BE around 530.5 eV in both samples consistent with literature values which are 530.4±0.5 eV [61,62,82-84,86]. The low BE shoulder at around 529.6 eV for both catalyst corresponds

to a contribution of CuO probably slightly modified (by Zn) since this value its slightly higher than the one expected (529.4 eV) [68]. A main high BE component η with a BE value of 531.4 eV for both catalysts which is slightly higher but consistent with the BEs of alumina, (Cu,Zn) aluminates or (Cu, Zn, Al) mixed oxides. Indeed alumina exhibits a broad range of BEs (531.0±1.0 eV) [67]; values for $ZnAl_2O_4$ [61,62,76], $CuAl_2O_4$ [61,62,66] and (Cu,Zn,Al) mixed oxides [61,62] are 531.1±0.3 eV (as previously, BE values were corrected by -0.5eV when the energy reference was 285.1eV for C1s and consequently 74.5 eV for Al2p). Together with the results for $Cu2p_{3/2}$ and $Zn2p_{3/2}$ this clearly indicates the presence of copper aluminates and that within oxides/aluminates there is an interaction between Cu and Zn with a more pronounced effect for the $C_{0.33}Z_{0.33}A_{0.33}$ catalyst; furthermore Cu(0) particles (again probably in interaction with Zn) exist for the two catalysts. The content of Cu and Zn on the surface varies according to the composition of the catalysts, which highlights the fact that the surface copper ratio between the solids studied ($C_{0.33}Z_{0.33}A_{0.33}/C_{0.44}Z_{0.22}A_{0.33}$ = 0.75) is identical to the total copper ratio in the materials (0.75), which indicates that, in these materials, the content distribution is rather homogenous from surface to bulk.

Figure 9 reports XRD peaks that confirm the presence of metallic copper particles in all the materials used, as well as copper oxide and zinc oxide, except in the $C_{0,33}Z_{0,33}A_{0,33}$ material, which failed to reach peaks assignable to CuO.

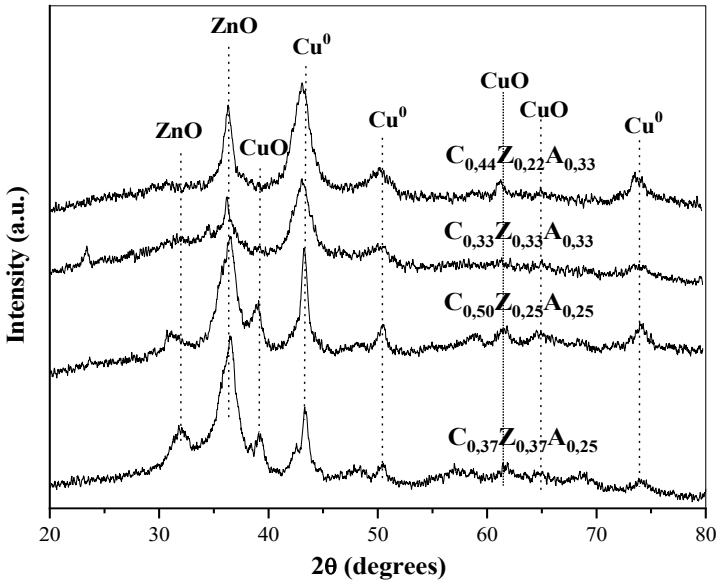

Figure 9. X-ray diffractograms of solids after of the catalytic evaluation.

The TOF indicates that this solid has a better performance, which can be ascribed to factors such as the smaller particle size of Cu^0 and to the presence of particles in which there are Cu-Zn interactions. Furthermore, the absence of CuO after catalytic evaluation indicates that the Cu^0 particles in this material are more resistant to oxidation, an effect that could have been induced by zinc and by the lower dispersion and metallic area displayed by this solid.

Conclusions

The calcination of the hydrotalcite-type precursors led to the formation of CuO particles in all the materials, which were more resistant to the reduction processes as the aluminum content augmented. All the catalysts displayed Cu^0 particles after the reduction process; however, the materials also contain CuO in their composition, except for the $C_{0.33}Z_{0.33}A_{0.33}$ material. The percentage of reaction increased with temperature, whereby the $C_{0.50}Z_{0.25}A_{0.25}$ and $C_{0.37}Z_{0.37}A_{0.25}$ materials were the most active with conversion rates nearing 90%. Through the TOF, it was observed that the $C_{0.33}Z_{0.33}A_{0.33}$ catalyst is the most effective depending on the copper content, which can be attributed to the absence of CuO, to the smaller size of the Cu^0 particles and, possibly, to the existence of Cu-Zn interactions on the surface of the solid.

Acknowledgements

EMF, JRR, thank the University of Cartagena and SENA for financial support. The authors acknowledge the financial support of CNPq, FINEP and PETROBRAS. S. Prakash is thanked for initial work on XPS.

References

1. A. Kubacka M. Fernández-García A. Martínez-Arias, Catalytic hydrogen production through WGS or steam reforming of alcohols over Cu, Ni and Co catalysts, *Applied Catalysis A: General*. 2016, **518**, pp. 2-17. https://doi.org/10.1016/j.apcata.2016.01.027
2. G. K.Reddy, P. G.Smirniotis, Water Gas Shift Reaction, *Research Developments and Applications*, 2015, pp. 1-20. Ed. Elsevier, China. https://doi.org/10.1016/B978-0-12-420154-5.00001-2
3. J.L. Santos, T.R. Reina, S. Ivanova, M.A. Centeno, J.A. Odriozola, Gold promoted $Cu/ZnO/Al_2O_3$ catalysts prepared from hydrotalcite precursors: Advanced materials for the WGS

reaction. *Applied Catalysis B: Environmental*. 2017, 201, pp. 310–317. http://doi.org/10.1016/j.apcatb.2016.08.017

4. N.K. Gamboa-Rosales, J.L. Ayastuy∗, M.P. González-Marcos, M.A. Gutiérrez-Ortiz, Effect of Au promoter in CuO/CeO_2 catalysts for the oxygen-assisted WGS reaction. *Catalysis Today.* 2011, 176 63– 71. https://doi.org/10.1016/j.cattod.2011.03.047
5. X. Lin, Y. Zhang, L. Yin, C. Chen, Y. Zhan, D. Li. Characterization and catalytic performance of copper-based WGS catalysts derived from copper ferrite. *International Journal of Hydrogen Energy*, 2014, 39 pp. 6424-6432. https://doi.org/10.1016/j.ijhydene.2014.02.018
6. C. Price, L.Pastor-Pérez, E. le Saché, A.Sepúlveda-Escribano, T.R.Reina, Highly active Cu-ZnO catalysts for the WGS reaction at medium–high space velocities: Effect of the support composition. *International Journal of Hydrogen Energy*. 2017, 42, pp. 10747-10751. https://doi.org/10.1016/j.ijhydene.2017.02.013
7. P. Pei, M. Wang, D. Chen, P. Ren, L. Zhang. Key technologies for polymer electrolyte membrane fuel cell systems fueled impure hydrogen. *Progress in Natural Science: Materials International*. 2020, 30, p. 751-763. https://doi.org/10.1016/j.pnsc.2020.08.015
8. J. Thomas, P. Edwards, P. Dobson, G. Owen. Decarbonising energy: The developing international activity in hydrogen technologies and fuel cells. *Journal of Energy Chemistry*. 2020, 51, pp. 405-415. https://doi.org/10.1016/j.jechem.2020.03.087
9. U. Khan, T. Yamamoto, H. Sato. Consumer preferences for hydrogen fuel cell vehicles in Japan. *Transportation Research Part D: Transport and Environment.* 2020, 87, pp. 102542. https://doi.org/10.1016/j.trd.2020.102542
10. S. M. Jokar, P. Parvasia, A. Basile. The evaluation of methane mixed reforming reaction in an industrial membrane reformer for hydrogen production, *International Journal of Hydrogen Energy*. 2018, 43, pp. 15321-15329. https://doi.org/10.1016/j.ijhydene.2018.06.142
11. M. Taji, M. Farsi, P. Keshavarz. Real time optimization of steam reforming of methane in an industrial hydrogen plant. *International Journal of Hydrogen Energy*. 2018, 43, pp. 13110-13121. https://doi.org/10.1016/j.ijhydene.2018.05.094
12. S. Sepehri, M. Rezaei, Y. Wang, A. Younesi, H. Arandiyan. The evaluation of autothermal methane reforming for hydrogen production over Ni/CeO_2 catalysts. 2018, 43, pp. 22340-22346. https://doi.org/10.1016/j.ijhydene.2018.10.016
13. B. Anzelmo, J. Wilcox, S. Liguori, Hydrogen production via natural gas steam reforming in a Pd-Au membrane reactor. Comparison between methane and natural gas steam reforming reactions. *Journal of Membrane Science*. 2018, 568, pp. 113–120. https://doi.org/10.1016/j.memsci.2018.09.054
14. Y.C. Pu, S.R. Li, S. Yan, X. Huang, D. Wang, Y.Y. Ye, Y.Q. Liu. An improved Cu/ZnO catalyst promoted by Sc2O3 for hydrogen production from methanol reforming. *Fuel*. 2019, 241, pp. 607–615. https://doi.org/10.1016/j.fuel.2018.12.067
15. Y. Zhang, P. Xu, S. Liang, B. Liu, Y. Shuai, B. Li. Exergy analysis of hydrogen production from steam gasification of biomass: A review. *International Journal of Hydrogen Energy*. 2019, 44, pp. 14290-14302. https://doi.org/10.1016/j.ijhydene.2019.02.064
16. D. Pashchenko. Experimental study of methane reforming with products of complete methane combustion in a reformer filled with a nickel-based catalyst. *Energy Conversion and Management*, 2019, 183, pp. 159-166. https://doi.org/10.1016/j.enconman.2018.12.102
17. W-H Chen, K-H Chen, B-J. Lin, YZ. Guo. Catalyst combination strategy for hydrogen production from methanol partial oxidation. *Energy*. 2020, 206, pp. 118180. https://doi.org/10.1016/j.energy.2020.118180

18. D. Raptis, A. K. Seferlis, V. Mylona, C. Politis, P. Lianos, Electrochemical hydrogen and electricity production by using anodes made of commercial aluminum, *International Journal of Hydrogen Energy*. 2019, 44, pp. 1359-1365. https://doi.org/10.1016/j.ijhydene.2018.11.202
19. L. Pastor-Perez, S. Gu, A. Sepúlveda-Escribano, T. Reina, Bimetallic CueNi catalysts for the WGS reaction-Cooperative or uncooperative effect?. *International Journal of Hydrogen Energy*. 2019, 44, pp. 4011-4019. https://doi.org/10.1016/j.ijhydene.2018.12.127
20. M. Zhu, I. Wachs. A perspective on chromium-Free iron oxide-based catalysts for high temperature water-gas shift reaction. *Catalysis Today*. 2018, 311, pp. 2-7. https://doi.org/10.1016/j.cattod.2017.08.042
21. T.K. Patra, S. Mukherjee, P.N. Sheth. Process simulation of hydrogen rich gas production from producer gas using HTS catalysis. *Energy*. 2019, 173, pp. 1130-1140. https://doi.org/10.1016/j.energy.2019.02.136
22. A. Arregi, M. Amutio, G. Lopez, J. Bilbao, M. Olazar. Evaluation of thermochemical routes for hydrogen production from biomass: A review. *Energy Conversion and Management*. 2018, 165, pp. 696-719. https://doi.org/10.1016/j.enconman.2018.03.089
23. M. Maroño, J.M. Sánchez, E. Ruiz. Hydrogen-rich gas production from oxygen pressurized gasification of biomass using a FeCr water gas shift catalyst. *International Journal of Hydrogen Energy*. 2010, 35, pp. 37-45. https://doi.org/10.1016/j.ijhydene.2009.10.078
24. N.K. Gamboa-Rosales, J.L. Ayastuy, M.P. González-Marcos, M.A. Gutiérrez-Ortiz. Effect of Au promoter in CuO/CeO_2 catalysts for the oxygen-assisted WGS reaction. *Catalysis Today*. 2011, 176, pp. 63-71. https://doi.org/10.1016/j.cattod.2011.03.047
25. M.J.L. Ginés, N. Amadeo, M. Laborde, C.R. Apesteguía. Activity and structure-sensitivity of the water-gas shift reaction over Cu-Zn-A1 mixed oxide catalysts. *Applied Catalysis A: General*, 1995, 131, pp. 283-296. https://doi.org/10.1016/0926-860X(95)00146-8
26. T.R. Reina, S. Ivanova, J.J. Delgado, I. Ivanov, V. Idakiev, T. Tabakova, M.A.Centeno, J.A. Odriozola. Viability of $Au/CeO_2–ZnO/Al_2O_3$ Catalysts for Pure Hydrogen Production by the Water–Gas Shift Reaction. *ChemCatChem*, 2014, 6, pp. 1401-1409. https://doi.org/10.1002/cctc.201300992
27. A. López Cámara, V. Cortés Corberán, A. Martínez-Arias, L. Barrio, R. Si, J.C. Hanson, J.A. Rodriguez. Novel manganese-promoted inverse CeO_2/CuO catalyst: In situ characterization and activity for the water-gas shift reaction. *Catalysis Today*, 2020, 339, pp. 24-31. https://doi.org/10.1016/j.cattod.2019.01.014
28. M.O. Souza, E.B. Quadro, M. Rangel. Propriedades texturais e catalÍticas de oxido de ferro contendo cromo e cobre. *Química Nova*, 1998, 21, pp.428-33. http://doi.org/10.1590/S0100-40421998000400010
29. A.O. Souza, G.C. Araujo, E.A. Pinheiro, M. Rangel. Efeito da temperatura no desempenho de catalisadores de óxidos de ferro contendo cobre e alumínio. *Química Nova*, 2002, 25, pp. 181-5. http://doi.org/10.1590/S0100-40422002000200002
30. A.C. Pereira, G.P. Berrocal, S. Marchetti, A. Albornoz, A. Souza, M. Rangel. A comparison between the precipitation and impregnation methods for water gas shift catalyst. Journal of Molecular Catalysis A: Chemical. 2008, 281, pp. 66-72. https://doi.org/10.1016/j.molcata.2007.07.042
31. D. Correia dos Santos, A.C. Oliveira, P.C. Morais, V.K. Garg, A.C. de Oliveira AC, M.L. Correa, M. Rangel. Evaluation of Fe/MCM-41 catalysts in the water gas shift reaction. *Studies in Surface Science and Catalysis*, 2004, 154, pp. 2417-2424. https://doi.org/10.1016/S0167-2991(04)80506-8
32. A. Romero-Núñez, A. Gómez-Cortés, H. Tiznado, G. Díaz. Ni-doped Ceria Nanorods for the WGS reaction: Effect of Ni distribution in methane suppression. *Catalysis Today*, 2020, 349, pp. 10-16. https://doi.org/10.1016/j.cattod.2018.09.009

33. N. García-Moncada, L. Jurado, M. Martínez-Tejada, F. Romero-Sarria, J. A. Odriozola. Boosting water activation determining-step in WGS reaction on structured catalyst by Mo-doping. *Catalysis Today*. Article in press. https://doi.org/10.1016/j.cattod.2020.06.003
34. T. Tabakova, I. Ivanov, R. Zanella, Y. Karakirova, J.W. Sobczak, W. Lisowski, Z. Kaszkur, L. Ilieva. Unraveling the effect of alumina-supported Y- doped ceria composition and method of preparation on the WGS activity of gold catalysts. *International Journal of Hydrogen Energy*. 2020, 45, pp. 26238-26253. https://doi.org/10.1016/j.ijhydene.2019.12.199
35. C. Lucarelli, C. Molinari, R. Faure, G. Fornasari, D. Gary, N. Schiaroli, A.Vaccari. Novel Cu-Zn-Al catalysts obtained from hydrotalcite-type precursors for middle-temperature water-gas shift applications. Applied Clay Science. 2018, 155, pp. 103-110. https://doi.org/10.1016/j.clay.2017.12.022
36. Y. Davoodbeygi, A. Irankhah. Catalytic characteristics of $Ce_xCu_{1-x}O_{1.9}$ catalysts formed by solid state method for MTS and OMTS reactions. *International Journal of Hydrogen Energy*. 2019, 44, pp. 16443-16451. https://doi.org/10.1016/j.ijhydene.2019.04.244
37. L. Pastor-Pérez, V. Belda-Alcázar, C. Marini, M. M. Pastor-Blas, A. Sepúlveda-Escribano, E. V.Ramos-Fernandez. Effect of cold Ar plasma treatment on the catalytic performance of Pt/CeO_2 in water-gas shift reaction (WGS). *Applied Catalysis B: Environmental*. 2018, 225, pp. 121-127. https://doi.org/10.1016/j.apcatb.2017.11.065
38. L P.C. Silva, M- M. Freitas, L. E. Terra, A.C.S.L.S. Coutinho, F. B.Passos. Preparation of $CuO/ZnO/Nb_2O_5$ catalyst for the water-gas shift reaction. *Catalysis Today*. 2020, 344, pp. 59-65. https://doi.org/10.1016/j.cattod.2018.10.028
39. E. Meza-Fuentes, M. Rangel. Síntesis de catalizadores de $Ni/ZnO/Al_2O_3$ para la reacción WGS a través del estudio de las propiedades estructurales y catalíticas de Ni/ZnO y Ni/Al_2O_3. *Revista Colombiana de Química*, 2011, 40, pp. 105-123. http://doi.org/10.15446/rev.colomb.quim
40. E. Meza, A. Faro, T. de Freitas, J. Assaf, M. Rangel, M. A comparison between copper and nickel-based catalysts obtained from hydrotalcite-like precursors for WGSR, *Catalysis. Today*, 2011, 171, 290. https://doi.org/10.1016/j.cattod.2011.03.082
41. E. Meza, F.J. Cadete Santos Aires, S. Prakash, A. Faro, T. de Freitas, J. Assaf, M. Rangel. The effect of metal content on nickel-based catalysts obtained from hydrotalcites for WGSR in one step, *International Journal of Hydrogen Energy*, 2014, 39, 815. https://doi.org/10.1016/j.ijhydene.2013.10.114
42. F. Cavani, F. Trifiro, A. Vaccari, Hydrotalcite-type anionic clays: preparation, properties and application, *Catalysis. Today*, 1991, 11, 173
43. J. Rodríguez-Ruiz, S. Osorio-Herrera, E. Meza-Fuentes. Effect of zinc substitution by nickel on hydrotalcite-type solids. *Revista Matéria*. 2020, 25, pp. 1-10. https://doi.org/10.1590/s1517-707620200002.1005
44. Y. Jugnet, D. Loffreda, C. Dupont, F. Delbecq, E. Ehret, F.J. Cadete Santos Aires, B.S. Mun, F. Aksoy Akgul, Z. Liu. Promoter Effect of Early Stage Grown Surface Oxides: A Near Ambient Pressure XPS Study of CO Oxidation on PtSn Bimetallics. *Journal of Physical Chemistry Letters*. 2012, 3, pp. 3707–3714. https://doi.org/10.1021/jz301802g
45. M.A. Languille, E. Ehret, H. C. Lee, C. K. Jeong, T. Ryo, H. Kondoh, K. Mase, Y. Jugnet, J.C. Bertolini, F.J. Cadete Santos Aires, B.S. Mun. In-situ surface analysis of AuPd(110) under elevated pressure of CO. *Catalysis Today*. 2016, 260, pp. 39–45. https://doi.org/10.1016/j.cattod.2015.05.029
46. K. Pattamakomsan, E. Ehret, F. Morfin, P. Gelin, Y. Jugnet, S. Prakash, J. Bertolini, J. Panpranot, F.J. Cadete Santos Aires. Selective hydrogenation of 1,3-butadiene over Pd and Pd–Sn catalysts supported on different phases of alumina. *Catalysis Today*. 2011, 164, pp. 28–33. https://doi.org/10.1016/j.cattod.2010.10.013
47. E. Ehret, E. Beyou, G.V. Mamontov, T.A. Bugrova, S. Prakash, M. Aouine, B. Domenichini, F.J. Cadete Santos Aires. Bimetallic PdAg nanoparticle arrays from

monolayer films of diblock copolymer micelles. *Nanoscale*. 2015, 7, pp. 13239–13248. https://doi.org/10.1039/c5nr02215k
48. A. Berthet, A.L. Thomann, F.J. Cadete Santos Aires, M. Brun, C. Deranlot, J.C. Bertolini, J.P. Rozenbaum, P. Brault, P. Andreazza. Comparison of Pd/(Bulk SiC) catalysts prepared by atomic beam deposition and plasma sputtering deposition: characterization and catalytic properties. *Journal of Catalysis*. 2000, 190, pp. 49–59. https://doi.org/10.1006/jcat.1999.2711
49. T. Caillot, Z. Salama, N. Chanut, F.J. Cadete Santos Aires, S. Bennici, A. Auroux. Hydrothermal synthesis and characterization of zirconia based catalysts. *Journal of Solid State Chemistry*. 2013, 203, pp. 79–85. https://doi.org/10.1016/j.jssc.2013.04.005
50. I. Grohmann, B. Peplinski, W. Unger, New entries in the XPS fingerprint database for the characterization of precipitated Cu-Zn-Al oxide catalysts. *Surface and Interface Analysis*. 1992, 19, pp. 591-594. https://doi.org/10.1002/ sia.7401901110
51. Y. Liu, Y. Gong, N.P. Mellot, B. Wang, H. Ye, Y. Wu, Luminescence of delafossite-type $CuAlO_2$ fibers with Eu substitution for Al cations. *Science and Technology of Advanced Materials*. 2016, 17, pp. 200-209. https://doi.org/10.1080/14686996.2016.1172024
52. J. Rodriguez-Ruiz, A. Pajaro-Payares, E. Meza-Fuentes, Síntesis y caracterización estructural de hidrotalcitas de Cu-Zn-Al. *Revista Colombiana de Química*. 2016, 45, pp. 33-38. https://doi.org/10.15446/rev.colomb.quim.v45n3.61381
53. U. Costantino, F. Marmottini, M. Sisani, T. Montanari, G. Ramis, G. Busca, M. Turco, G. Bagnasco. Cu-Zn-Al hydrotalcites as precursors of catalysts for the production of hydrogen from methanol. *Solid State Ionics*. 2005, 176, pp. 2917-2922. https://doi.org/10.1016/j.ssi.2005.09.051
54. S. Kannan, V. Rives, H. Knözinger. High-temperature transformations of Cu-rich hydrotalcites. J. *Journal of Solid State Chemistry*, 2004, 177, pp. 319-331. https://doi.org/10.1016/j.jssc.2003.08.023
55. K. Sing, D. Everett, R. Haul, L. Moscou, R. Pierotti, J. Rouquerol. Reporting physisorption data for gas/solid systems, with special reference to the determination of surface area and porosity. *Pure and Applied Chemistry*. 1985, 57, pp. 603-619. https://doi.org/10.1351/pac198557040603
56. S. Gentry, N. Hurst, A. Jones. Temperature programmed reduction of copper ions in zeolites. *Journal of the Chemical Society, Faraday Transactions 1*, 1979, 75, pp. 1688- 1699.
57. D. Hoang, T. Dang, J. Engeldinger, M. Schneider, J. Radnik, M. Richter, A. Martin. TPR investigations on the reducibility of Cu supported on Al_2O_3, zeolite Y and SAPO-5. *Journal of Solid State Chemistry*. 2011, 184, pp. 1915-1923. https://doi.org/10.1016/j.jssc.2011.05.042
58. E. Meza-Fuentes, J. Rodríguez-Ruiz, C. Solano-Polo, M. Rangel, A. Faro, Monitoring the structural and textural changes of Ni-Zn-Al hydrotalcites under heating, Thermochimica Acta, 2020, 687, 78594. https://doi.org/10.1016/j.tca.2020.178594
59. K. R. Gunugunuri, G. S. Panagiotis. (2015). Water Gas Shift Reaction, Research Developments and Applications, Chapter 3- Low Temperature WGS Reaction, pp. 47-100. https://doi.org/10.1016/B978-0-12-420154-5.00003-6
60. G. Moretti, P. Porta, Charge distribution and local and non-local screening effects studied by means of the Auger parameter and chemical state plots. *Surface and Interface Analysis*.1990, 15, pp. 47-50. https://doi.org/10.1002/sia.740150108
61. G. Moretti, XPS studies of characterized Cu/Al_2O_3, Zn/Al_2O_3 and $Cu-Zn/Al_2O_3$ catalysts. *Surface and Interface Analysis*.1991, 17, pp. 745-750. https://doi.org/10.1002/sia.740171009
62. P. Porta, M.C. Campa, G. Fierro, M. Lo Jacono, G. Minelli, G. Moretti, L. Stoppa, CuO-ZnO-Al_2O_3 mixed oxides: preparation, bulk and surface characterization. *Journal of Materials Chemistry*. 1993, 3, pp. 505-511. https://doi.org/10.1039/jm9930300505
63. S. Velu, K. Suzuki, C.S. Gopinath, H. Yoshida, T. Hattori, XPS, XANES and EXAFS investigations of $CuO/ZnO/Al_2O_3/ZrO_2$ mixed oxide catalysts. *Physical Chemistry Chemical Physics*. 2002, 4, pp. 1990–1999. https://doi.org/10.1039/b109766k

64. R.M. Friedman, J.J. Freeman, F.W. Lytle, Characterization of Cu/Al_2O_3 catalysts. *Journal of Catalysis*. 1978, 55, pp. 10-28. https://doi.org/10.1016/0021-9517(78)90181-1
65. G. Ertl, R. Hierl, H. Knözinger, N. Thiele, H.P. Urbach, XPS study of copper aluminate catalysts. *Applications of Surface Science*. 1980, 5, pp. 49-64. https://doi.org/10.1016/0378-5963(80)90117-8
66. B.R. Strohmeier, D.E. Leyden, R.S. Field, D.M. Hercules, Surface spectroscopic characterization of Cu/Al_2O_3 catalysts. *Journal of Catalysis*. 1985, 94, pp. 514-530. https://doi.org/10.1016/0021-9517(85)90216-7
67. J.F. Moulder, W.E. Stickle, P.E. Sobol, K.D. Bomben, *in* Handbook of X-ray Photoelectron Spectroscopy. J. Chastian (Ed.), Perkin-Elmer Corp., Minnesota, 1992.
68. R.P. Vasquez, CuO by XPS. *Surface Science Spectra*. 1998, 5, pp. 262-266. http://doi.org/10.1116/1.1247882
69. M.C. Biesinger, Advanced analysis of copper X-ray photoelectron spectra. *Surface and Interface Analysis*. 2017, 49, pp. 1325-1334. http://doi.org/10.1002/sia.6239
70. J.P. Espinós, J. Morales, A. Barranco, A. Caballero, J.P. Holgado, A.R. González-Elipe, Interface effects for Cu, CuO, and Cu_2O deposited on SiO_2 and ZrO_2. XPS determination of the valence state of copper in Cu/SiO_2 and Cu/ZrO_2 catalysts. *Journal of Physical Chemistry B*. 2002, 106, pp. 6921-6926. http://doi.org/10.1021/jp014618m
71. M.C. Biesinger, L.W.M. Lau, A.R. Gerson, R.St.C. Smart, Resolving surface chemical states in XPS analysis of first row transition metals, oxides and hydroxides: Sc, Ti, V, Cu and Zn. Applied Surface Science. 2010, 257, pp. 887-898. http://doi.org/10.1016/j.apsusc.2010.07.086
72. S. Poulston, P. M. Parlett, P. Stone, M. Bowker, Surface oxidation and reduction of CuO and Cu_2O studied using XPS and XAES. *Surface and Interface Analysis*. 1996, 24, pp. 811-820. https://doi.org/10.1002/(SICI)1096-9918(199611)24:12<811::AID-SIA191>3.0.CO;2-Z
73. R.P. Vasquez, $Cu[OH)_2$ by XPS. *Surface Science Spectra*. 1998, 5, pp. 267-272. http://doi.org/10.1116/1.1247883
74. R.P. Vasquez, Cu_2O by XPS. *Surface Science Spectra*. 1998, 5, pp. 257-261. http://doi.org/10.1116/1.1247881
75. A.C. Miller, G.W. Simmons, Copper by XPS. *Surface Science Spectra*. 1993, 2, pp. 55-60. https://doi.org/10.1116/1.1247725
76. B.R. Strohmeier, D.M. Hercules, Surface spectroscopic characterization of the onteraction between zinc ions and γ-alumina. *Journal of Catalysis*. 1984, 86, pp.266-279. https://doi.org/10.1016/0021-9517(84)90372-5
77. R. Lindsay, G. Thornton, Structure of atomic and molecular adsorbates on low-Miller-index ZnO surfaces using X-ray absorption spectroscopy. *Topics in Catalysis*. 2002, 18, pp.15-19. https://doi.org/10.1023/A:1013821915062
78. N. Rößler, V. Staemmler, Ab initio calculations for the 2s and 2p core level binding energies of atomic Zn, Zn metal, and Zn containing molecules. *Physical Chemistry Chemical Physics*. 2003, 5, pp. 3580–3586. https://doi.org/10.1039/b302801a
79. N. Rössler, K. Kotsis, V. Staemmler, Ab initio calculations for the Zn 2s and 2p core level binding energies in Zn oxo compounds and ZnO. *Physical Chemistry Chemical Physics*. 2006, 8, pp. 697–706. https://doi.org/10.1039/b512379h
80. Ch. Wöll, The chemistry and physics of zinc oxide surfaces. *Progress in Surface Science*. 2007, 82, pp. 55-120. https://doi.org/10.1016/j.progsurf.2006.12.002
81. S. Bera, S. Dhara, S. Velmurugan, A.K. Tyagi, Analysis on binding energy and Auger parameter for estimating size and stoichiometry of ZnO nanorods. *International Journal of Spectroscopy*. 2012, 371092, pp. 1-4. https://doi.org/10.1155/2012/371092
82. Y. Okamoto, K. Fukino, T. Imanaka, S. Teranishi, Surface characterization of CuO-ZnO methanol-synthesis catalysts by X-ray photoelectron spectroscopy. 1. Precursor and calcined catalysts. *The Journal of Physical Chemistry*. 1983, 87, pp. 3740-3747. https://doi.org/10.1021/j100242a034

83. Y. Okamoto, K. Fukino, T. Imanaka, S. Teranishi, Surface characterization of CuO-ZnO methanol-synthesis catalysts by X-ray photoelectron spectroscopy. 2. Reduced catalysts. *The Journal of Physical Chemistry*. 1983, 87, pp. 3747-3754. https://doi.org/10.1021/j100242a035
84. D. Xu, D. Fan, W. Shen, Catalyst-free direct vapor-phase growth of $Zn_{1-x}Cu_xO$ micro-cross structures and their optical properties. *Nanoscale Research Letters*. 2013, 8, 46 (pp. 1-9). https://doi.org/10.1186/1556-276X-8-46
85. C.D. Wagner, Auger parameter in electron spectroscopy for the identification of chemical species. *Analytical Chemistry*. 1975, 47, pp.1201-1203. https://doi.org/10.1021/ac60357a021
86. M. Kunat, St.G. Girol, Th. Becker, U. Burghaus, Ch. Wöll, Stability of the polar surfaces of ZnO: a reinvestigation using He-atom scattering. *Physical Review B*. 2002, 66, 081402(R) (pp.1-3). https://doi.org/10.1103/PhysRevB.66.081402